Materials Science & Engineering A 918 (2024) 147475

Contents lists available at ScienceDirect

Materials Science & Engineering A

journal homepage: www.elsevier.com/locate/msea

Data-driven inverse design of MoNbTiVWZr refractory multicomponent alloys: Microstructure and mechanical properties

Lavanya Raman [a,1,*], Arindam Debnath [a], Erik Furton [a], Shuang Lin [a], Adam Krajewski [a], Subrata Ghosh [a], Na Liu [a], Marcia Ahn [a], Bed Poudel [a], Shunli Shang [a], Shashank Priya [a], Zi-Kui Liu [a], Allison M. Beese [a,b], Wesley Reinhart [a], Wenjie Li [a,**]

[a] Department of Materials Science and Engineering, Pennsylvania State University, University Park, PA, 16802, USA
[b] Department of Mechanical Engineering, Pennsylvania State University, University Park, PA, 16802, USA

ARTICLE INFO

Keywords:
Refractory multicomponent alloys
Data-driven inverse design
CALPHAD
Heterogeneous
Mechanical properties

ABSTRACT

Multicomponent refractory alloys have the potential to operate in high-temperature environments. Alloys with heterogeneous/composite microstructure exhibit an optimal combination of high strength and ductility. The present work generates designed compositions using high-throughput computational and machine-learning (ML) models based on elements Mo-Nb-Ti-V-W-Zr manufactured utilizing vacuum arc melting. The experimentally observed phases were consistent with CALPHAD and Scheil simulations. ML models were used to predict the room temperature mechanical properties of the alloy and were validated with experimental mechanical data obtained from the three-point bending and compression tests. This work collectively showcases a data-driven, inverse design methodology that can effectively identify new promising multicomponent refractory alloys.

1. Introduction

The development of refractory multicomponent alloys (RMCAs) with high concentrations of group IV (Ti, Zr, Hf), V (V, Nb, Ta), and VI (Cr, Mo, W) alloying elements has gained significant attention due to their impressive combinations of properties such as high temperature strength, wear resistance, and thermal stability [1]. While RMCAs excel at temperatures exceeding 1200 °C due to their high melting temperature and strength retention, their limited ductility at room temperature and high density restrict their application as structural materials. To address this challenge, a heterogeneous composite microstructure comprising hard and soft phases has emerged as a practical approach to achieve an optimum balance of high strength and ductility [2–4]. However, obtaining a desired combination of properties, such as strength, density, ductility, thermal stability, fatigue/creep resistance, and oxidation resistance, for any targeted application from a single alloy composition remains a significant challenge. Recent advancements in non-equiatomic MCAs have expanded the compositional space for alloy design, offering a promising avenue for enhancing mechanical properties beyond equiatomic MCAs [5,6]. Although non-equiatomic MCAs provide a vast landscape for alloy design, predicting phases and properties within this space requires advanced techniques and theories. Recent studies have demonstrated outstanding mechanical properties in non-equiatomic MCAs, highlighting their potential for various high-temperature applications. Efforts to develop optimal materials with tailored properties for specific applications are still highly desired, emphasizing the need for advanced predictive tools to streamline the material development process and reduce time, energy, and cost investments [7–9].

The convergence of experimental and computational methods, coupled with the rising popularity of data-driven approaches, have spurred the adoption of machine learning (ML) techniques in materials design. Leveraging vast datasets from techniques like Density Functional Theory (DFT) and CALculation of PHAse Diagram (CALPHAD), ML facilitates the development of surrogate models capable of predicting material properties based on factors such as crystal structure, composition and processing history [10–17]. One prevalent approach involves building surrogate models for forward design, enabling the exploration of chemical space to identify candidates with target properties. These models, often combined with optimization algorithms, streamline the

* Corresponding author.
** Corresponding author.
E-mail addresses: lraman@wisc.edu, lavanya.metly@gmail.com (L. Raman), wzl175@psu.edu (W. Li).
[1] Present email address.

https://doi.org/10.1016/j.msea.2024.147475
Received 17 June 2024; Received in revised form 30 September 2024; Accepted 27 October 2024
Available online 28 October 2024

search for candidate materials that meet specific criteria. In contrast, emerging methods, such as Variational Autoencoders (VAEs) and Generative Adversarial Networks (GANs) using generative models, enable inverse design by learning to approximate property distributions. This allows for the rapid generation of new material candidates in a single iteration, bypassing the need for iterative surrogate model searches in forward design approaches.

Among the RMCA literature, HfNbTaTiZr exhibits a stable microstructure and an optimum combination of high-temperature strength and ductility (>50 %) up to 1200 °C [18,19]. Later, lightweight RMCAs with Cr addition, such as Cr-Nb-Ti-V-Zr, were developed to improve the oxidation resistance and reduce density. However, the Cr in RMCAs promotes the formation of the Laves phase, increasing the alloys' strength at the expense of ductility [20,21]. Subsequently, Mo has been introduced as a replacement for Cr in alloys like Mo-Nb-Ti-V-Zr and Mo-Nb-Ta-Ti-W, aiming to improve strength and stability at elevated temperatures. The addition of Zr in these alloys induces positive enthalpy of mixing, leading to phase separation, reduces the valence electron configuration (VEC) that lowers the intrinsic brittleness, and causes lattice distortion due to larger atomic radius. Further enhancements in high-temperature strength are achieved by incorporating Mo and W [19,22]. In MoNbTaW-based alloys, including V and Zr, along with Mo and W, have been found to contribute to adequate strength and ductility through lattice misfit mechanisms [23].

This study generates high-entropy compositions based on the Mo-Nb-Ti-V-W-Zr alloy system from the ULTERA database by high-throughput computational and machine-learning models. The chosen compositions were fabricated via vacuum arc melting, and the observed phases were compared with CALPHAD and Scheil simulations. The mechanical properties such as hardness, Young's modulus, and maximum compressive strength predicted using ML algorithms were validated with experimental data. Further, comparisons of microstructure and mechanical behavior were made with other RMCAs and refractory alloys. Our work demonstrates a practical inverse design approach for identifying, fabricating, and validating promising candidates of other multicomponent alloys.

2. Materials and methods

2.1. Surrogate models

The design of RMCAs must consider multiple potentially conflicting property requirements, such as thermodynamic and mechanical descriptors, along with density and cost that affect their application. Thermodynamic descriptors include the ideal entropy of mixing (ΔS_{mix}), which identifies the added stability with an increasing number of constituents when present in equimolar fractions, and the D parameter, which is the ratio of surface energy versus unstable stacking fault energy, indicates ductility. Mechanical parameters include fracture toughness, compressive strength (CS) at room temperature (RT), and hardness. Each property requires different testing apparatuses; some of these tests are destructive, making it time-consuming and expensive to obtain all the relevant measurements. Apart from being used for forward design, surrogate models can provide a rapid and cost-effective alternative to extensive experimental or computational validation. Therefore, for this study, we have utilized surrogate models for each descriptor, which broadly fall under these categories, namely heuristic, phenomenological, and data-driven ML models, and are explained in the supplementary section S1. We have utilized ML surrogate models to predict the hardness and CS of the MCAs. The datasets used for training the ML surrogate models in this study were taken from the ULTERA Database, a curated database developed as a part of the ULTIMATE program of the U.S. Department of Energy (DOE) [24].

Input data for training the hardness surrogate model was restricted to RT tests in an as-cast (AC) state. This yielded a training dataset of 649 unique experimental property data points (643 from previously published work from the ULTERA Database + 6 new MoNbW alloys from our previous work [25]). The ML model used was an implementation of the Multi-Layer Perceptron (MLP) regressor from the sklearn python package, using standardized input features and hardness values. The compositions were represented as a 103-dimensional vector array (the composition vector), with each vector component carrying the atomic fraction of one of the first 103 elements from the periodic table. The decision was motivated by results from a previous study that indicated that the transfer learning features, like General and Transferrable Deep Learning (GTDL) from Feng et al., do not outperform atomic fractions as inputs [26,27]. The MLP's hyperparameters were tuned using grid search and 10-fold cross-validation of the entire training dataset. The 10 models from cross-validation were then used to obtain the average prediction and uncertainty.

We used an MLP regressor to predict the compressive strength of an alloy, using the composition vector, processing conditions, phases, and test temperature (in Kelvin) as the input features. The processing condition was represented as binary categories of either as-cast or heat-treated depending on the postprocessing of the alloy. The phase of the alloys was also categorized into one of the three classes: pure single-phase solid solution, a mixture of solid solutions/intermetallics, or amorphous. The processing conditions and the phase were then converted to one-hot encoded vectors, and the temperature was concatenated to the composition vector. An additional feature selection was performed to reduce the number of features being used as input to the model. For this purpose, the 21 selected features from the list of 118 initial features include a) the atomic fractions for elements Al, Co, Cr, Fe, Mn, Mo, Nb, Ni, Ta, Ti, V, W, Zr; b) the test temperature; c) two binary features to indicate the manufacturing process - one for hot rolling (HR), and another for spark plasma sintering (SPS); d) a binary feature to indicate the sample condition – as cast or annealed; e) three binary features to suggest the observed phase - BCC, FCC, or intermetallics (IM); f) a binary feature that indicates if the sample forms a single-phase solid solution.

The dataset used for training the CS surrogate model was obtained from the ULTERA database [24]. It contains 726 composition-processing-structure-property data points, with 326 unique compositions. Like before, the model's hyperparameters were selected using grid search and 10-fold cross-validation, and the predictions from the 10 models from cross-validation were used to obtain the mean and standard deviation in CS.

2.1.1. Synthetic dataset

Deep learning models like GANs typically require a large training dataset (approximately 10^4-10^6 data points). However, most materials science datasets are much smaller in scale since generating large amounts of data from experiments and simulations is expensive and time-consuming. Since these smaller datasets should not be used directly for deep learning, an alternative would be to construct and use a larger dataset by combining the design of experiments and surrogate models. Therefore, in this study, we constructed a synthetic dataset of MCA compositions formed by combining the 9 refractory elements (Cr, Hf, Mo, Nb, Ta, Ti, V, W, and Zr) in different proportions (with a minimum step of 1 %) to form binaries to senary systems. While the composition space formed from these elements would constitute $\sim 3^{11}$ alloys, the constructed synthetic dataset has ~800,000 compositions, which is less than 0.0003 % coverage of the compositional space. The properties of the synthetic compositions were calculated using the surrogate models discussed in the previous section.

2.1.2. Inverse design using conditional Generative Adversarial Networks (cGANs)

GANs can learn a mapping between complex, high-dimensional design space to a simple, lower-dimensional latent space that captures the underlying data distribution in the original space. The GAN architecture consists of two deep neural networks (DNNs) that are trained in

tandem – a generator (G) that creates realistic-looking synthetic/artificial samples from random noise drawn from a normally distributed latent space and a discriminator that learns to distinguish between samples from the real domain or generator. In particular, the conditional variant of GANs, called conditional GANs or cGANs, are theorized to be especially applicable for inverse design due to their capability to control the output of the generator by using some auxiliary information (or conditioning vector) as additional input to the generator and the discriminator. Modifying the architecture ensures that the generator obtains the context to learn a multi-model mapping from the input to the output domain.

In continuation of our previous work, where we demonstrated that a cGAN can be used for the inverse design [25], here we aim to design MCAs that simultaneously satisfy multiple design criteria using the synthetic dataset. We are particularly interested in MCAs with an optimum combination of density and strength. Therefore, we applied a cGAN with 4 fully connected layers (3 hidden layers + 1 output layer) conditioned on seven properties of interest: ΔS_{mix}, fracture toughness, D parameter, price, density, CS, and hardness. While there are no explicit criteria that need to be satisfied for ΔS_{mix}, hardness, or cost, including them in the conditioning allows the manipulation of the output from the cGAN. For instance, it would also be desirable if the alloy was designed to be as affordable as possible. The empirical probability distribution of the standardized property values was used to sample the conditioning values. The input to the generator is an 11-dimensional vector (4 corresponding to the random noise + 7 corresponding to the properties), with the output being a 9-dimensional composition vector. Each component of the composition vector corresponds to the atomic fraction of a particular element in the design space. The learning rates of both the generator and the discriminator were set to 10^{-3}. The models were implemented and trained using the Pytorch Python package. Incorporating additional features to the cGAN conditioning is efficient but only requires retraining the model.

2.2. Alloy synthesis

The designed Mo-Nb-Ti-V-W-Zr samples were fabricated using vacuum arc melting (VAM) (MAM-1, Edmund Buehler, GmbH). Wires of W, Mo, and Nb, Ti foils and V, Zr granules (all >99.8 %, Sigma Aldrich) were weighed stoichiometrically as $Mo_{13}Nb_{47}Ti_3V_{13}W_7Zr_{17}$ (alloy A) and $Mo_{20.3}Nb_{27.8}Ti_{6.5}V_{24.1}W_{6.2}Zr_{15.1}$ (alloy B) with a total mass of 15 g. To ensure complete mixing and homogeneity, the ingots were overturned and re-melted 10 times with an arc holding time of 1 min/melting cycle. The as-cast ingots had a lustrous surface with a diameter between 15 and 18 mm and a thickness of 7–9 mm. The as-cast ingots were further annealed at 1400 °C for 48 h by sealing them in a quartz tube under vacuum (~10^{-5} mbar), followed by furnace cooling.

2.3. Structural and mechanical characterization

The crystal structure of coupon samples was confirmed using X-ray diffraction (XRD, PANalytical X-ray Diffractometer, Malvern Panalytical Ltd.) with Cu K_α radiation and a Bragg–Brentano configuration over a 2θ range between 30 and 80°. Instrumental broadening was corrected using a silicon standard reference material. The lattice parameter of the as-cast alloys was analyzed using the Nelson-Riley (N. R.) function [28]. The microstructures of the alloys were characterized by field emission scanning electron microscopy (FESEM, FEI Verios G4, Thermo Fisher Scientific), energy dispersive spectroscopy (EDS, Oxford Aztec), and electron backscattered diffraction (EBSD, FEI Apero S, Thermo Fisher Scientific). The EBSD analysis was carried out with a step size of 0.4 mm using Oxford Aztec Crystal software with an equivalent circle diameter method for grain size analysis and TruPhase (Oxford Aztec) for phase analysis. The Vickers microhardness of the RMCAs was measured (Leco V-100-C1, Leco Corporation) using a load of 500 g with a dwell time of 10 s. The average value of ten measurements was reported for each sample.

Room temperature compression and three-point bending tests were performed using an axial mechanical load frame (MTS Criterion 43, Criterion 45, MTS Systems). For three-point bending, at least two thin bars were extracted for each composition from pucks using wire EDM and were subsequently mechanically polished, with dimensions of 1.5 mm × 1 mm × 15 mm. The length between the outer pins was 12 mm, and the crosshead displacement rate was 0.0050 mm/s, resulting in a strain rate at the outer fiber at the center of the sample of $2 \times 10^{-4}\ s^{-1}$. For the bending tests, digital image correlation confirmed that all macroscopic deformation was linear-elastic. Therefore, the bending strength, critical failure strain, and elastic modulus were calculated using the Euler-Bernoulli beam theory. For compression tests, a rectangular cuboid of $4 \times 4 \times 6\ mm^3$ was used, with a strain rate of $4 \times 10^{-4}\ s^{-1}$, and two samples were tested for each composition.

The RT nanoindentation (NI) experiments were carried out on a Hysitron TI 950 TriboIndenter (Bruker Corporation, Billerica, Massachusetts, USA) with a Berkovich indenter to obtain the individual phase/region hardness. Accelerated property mapping (XPM) was acquired from a matrix of 10 × 10 indents (5 μm spacing between consecutive indents). Tests were performed under constant load mode with a peak load of 5000 μN (0.5 s loading, 0.2 s holding, and 0.5 s unloading). Poisson's ratio of 0.3 was assumed to obtain the elastic and shear modulus from the measured reduced modulus.

2.4. CALPHAD-based thermodynamic calculation and scheil simulation

We used the CALPAHD approach to predict equilibrium phases and solidification behavior using Thermo-Calc software [29,30] in combination with the TCHEA database. The employed thermodynamic database of the Mo-Nb-Ti-V-W-Zr system was combined from previous works [31–43], which includes the BCC, HCP, LAVES (C15), and liquid phases. Both equilibrium calculations and Scheil model simulations were performed for the two designed alloys. Equilibrium calculations minimize the Gibbs energy for the system of interest. The Scheil solidification model was first introduced by Gulliver and Scheil [44]. The model considers the following assumptions: 1) perfect mixing of liquid with infinite diffusivity; 2) no diffusion in the solid phase; and 3) local equilibrium between liquid and solid at the solid/liquid interface.

3. Results and discussion

3.1. Composition identification from ML

The trained generator was tasked with generating multiple candidate compositions with the desired property values (with value for $\Delta S_{mix} \sim$ 1.5R, an arbitrarily chosen low cost, and an arbitrarily chosen high value of the hardness), out of which the composition $Mo_3Nb_6Ti_{30}V_3W_{27}Zr_{30}$ was selected based on the predictions of the surrogate models. However, unmelted W regions were observed during arc melting. Given the high content of W, one possible way to mitigate this issue was to reduce the amount of W in the composition. As W content is not a part of the conditioning properties, it is not trivial to induce the generator to generate new compositions with W content within a specific range. In contrast, it is possible to perform operations in the latent space to manipulate the generator's output and derive a composition with the necessary content of W [27,45]. A multi-objective optimization using the pymoo python package was used, where a local optimization reduced W content while maximizing UTS at 1200 °C, fracture toughness, and hardness while minimizing price. Constraints included the atomic fractions summing to unity and density ~ 8–10 g cm^{-3}. Upon optimization, the composition $Mo_{20.3}Nb_{27.8}Ti_{6.5}V_{24.1}W_{6.2}Zr_{15.1}$ was obtained.

Apart from generating compositions from the cGAN, a forward search was also performed on the synthetic dataset with the necessary

search conditions, as described in Section 2.1.1. Based on the search, we were able to select the composition $Mo_{13}Nb_{47}Ti_3V_{13}W_7Zr_{17}$ from the shortlisted candidates. The compositions $Mo_{13}Nb_{47}Ti_3V_{13}W_7Zr_{17}$ and $Mo_{20.3}Nb_{27.8}Ti_{6.5}V_{24.1}W_{6.2}Zr_{15.1}$ are designated as Alloy A and B, respectively. A summary of the predicted properties for the alloys A and B using the surrogate models is shown in Table 1.

3.2. Microstructure

The XRD pattern of the as-cast and annealed alloys A and B exhibit two BCC solid solutions and a secondary Laves phase, as shown in Fig. 1 (a). The BCC1 phase of the alloys A and B is Zr-rich, with a lattice parameter of 0.3615 nm and 0.3549 nm, respectively, whereas the BCC2 phase is W-rich, with a lattice parameter of 0.3266 nm and 0.3204 nm, respectively. Both the alloys have similar phases, and the difference in the lattice parameters can be attributed mainly to the differences in the Mo, Nb, and V concentrations, which shift the peaks (corresponding to the BCC phases of alloy B) to higher angles, indicating a reduced lattice parameter.

The phases detected through XRD were correlated with SEM analysis, as shown in Fig. 1(b). The microstructure of annealed samples exhibits dendritic (D) and interdendritic (ID) regions due to the difference in the melting point of the elements. The high melting point elements, such as Mo and W, segregate in the D regions, whereas the relatively low melting point element Zr concentrates in the ID region. Correlating Figs. 1(b) and 2(a), it is indicative that the grey region (indicated by blue arrow) surrounding the dark ID region (indicated by yellow arrow) is rich in Nb and V. The dark ID region is Zr-rich, corresponding to the BCC1 phase, whereas the matrix (bright region indicated by red arrow) is Zr-depleted, corresponding to the BCC2 phase. The composition of different regions of alloys A and B, quantified using SEM-EDS analysis, is given in Fig. 2(b).

Moreover, the BCC2 phase consists of a homogenous distribution of Zr-rich fine precipitates (Fig. 1(b), consistent with the Nb-Mo-Zr-based alloys [46]. The distribution of different phases, along with the IPF map and elemental mapping for alloys A and B obtained from EBSD analysis, is shown in Fig. 3. The microstructure of alloys A and B is similar with the presence of similar phases, which differs in their lattice parameter due to the variation in their composition. The volume fraction of the phases obtained from SEM analysis is given in supplementary section S2.

3.3. Thermodynamic equilibrium and non-equilibrium scheil predictions

The preceding microstructural analysis shows that alloys A and B comprise two BCC solid solutions with a secondary Laves phase. Fig. 4 displays the equilibrium phase fraction predictions of the two designed alloys, A and B, as functions of temperature. Alloy A exhibits liquid, HCP, C15, and two BCC phases (BCC#1 and BCC#2) in the equilibrium calculation, while alloy B predominantly consists of liquid, two BCC phases, and the C15 phase. The phase transformation temperatures for both alloys are summarized in Supplementary section S3. For alloy A, both equilibrium and Scheil simulations indicate the formation of only the BCC#2 phase during solidification.

On the other hand, for alloy B, the equilibrium simulation suggests the formation of the BCC#2 phase, while the Scheil simulation indicates the formation of the C15 phase at around 1200 °C. Alloy A displays higher phase transition temperatures in the start temperature from liquid to the BCC#2 phase (T_L) and completion from liquid to the BCC#2 phase (T_S). As temperature decreases, the BCC#2 phase partially transforms into BCC#1 phase at 1215 °C in alloy A, followed by a transformation into HCP and C15 phases at 615 °C and 550 °C, respectively. Conversely, in alloy B, the BCC#2 phase partially transforms into the C15 phase at 1205 °C before transforming into C15 and BCC#1 at 830 °C. The higher fraction of C15 phase in alloy B aligns with the SEM experimental findings. Fig. 4(c) shows the equilibrium and Scheil solidification simulation of alloys A and B. It is observed that the range of equilibrium solidification is much narrower than that of Scheil solidification, resulting in the formation of the BCC#2 phase.

Moreover, it is essential to note the solidification sequence in both alloys. The BCC#2 phase (W-rich) solidifies first, followed by BCC#1(Zr-rich) and C15 Laves phase in both the alloys, which is consistent with the experimental observation of W-rich dendrites and Zr-rich interdenrites. The phase composition of the alloys at different temperatures is mentioned in Supplementary section S3.

Table 1
Predicted properties of designed alloys A and B obtained from surrogate models.

Alloy	ΔS_{conf} (J/K)	D parameter (−)	Price ($/g)	Density (g/cm^3)	Hardness (GPa)	CYS (GPa)
A	1.48R	2.97	84.9	7.76	4.07 ± 0.19	1.63 ± 0.12
B	1.66R	2.61	133.3	8.32	6.04 ± 0.19	1.77 ± 0.11

3.4. Phase formation criteria

The alloys studied are multiphase in nature with a dendritic microstructure. The experimentally observed phases are consistent with the CALPHAD predictions. Both the alloys show the presence of two BCC phases and a Laves phase. CALPHAD and Scheil simulations indicate that the alloys have a wide solidification range of approximately 800 °C. In both alloys, the high temperature BCC solid solution dissociates into low temperature BCC solid solution and a C15 Laves phase. Similar observations are reported for Mo_xNbTiV_yZr RMCAs [47]. The presence of Zr results in an increased segregation tendency with strong segregation of Zr in the ID regions due to its positive ΔH_{mix}. The calculated empirical parameters for phase formation criteria in MCAs are also used to explore phase evolution. The values of various parameters such as entropy of mixing, enthalpy of mixing, omega parameter, size difference, atomic packing factor, electronegativities (Allen, $\Delta\chi_A$ and Pauling, $\Delta\chi_P$) and VEC are as given in Table 2.

Different interactions between the alloying elements are responsible for the phase separation. The hexanary Mo-Nb-Ti-V-W-Zr system contains fifteen binary and twenty ternary systems. Among the binaries, Ti-V, Nb-V, Ti-V, Ti-Mo, and W-V exhibit a miscibility gap, and interaction of Zr with the other elements results in the HCP + C15 Laves phase. These binary and ternary interactions reflect in the higher-order hexanary system and result in the separation of the high-temperature BCC phase into BCC and Laves phase at temperatures below 1200 °C. Both alloys show the formation of two disordered BCC phases. One is rich in Zr, lean in Nb (BCC2), and another is rich in Nb and depleted in Zr (BCC1), consistent with CALPHAD predictions. Moreover, the Laves phase formation in these alloys can be attributed to the atomic radius difference between V and Zr, which is the largest among the alloying elements. From Table 2, the atomic packing parameter and the electronegativity parameter also indicate the formation of the Laves phase along with BCC solid solutions.

3.5. Mechanical properties

3.5.1. Vickers hardness: correlation between experiment and prediction

The predictions from the ML models were assessed and compared to the experimental results. A lower value of RMSE and a higher value of R^2 indicate that the model's predictions were more aligned with the measured values. The 10-hardness model ensemble had a mean RMSE of 0.76 GPa and an R^2 score of 0.84. The experimental Vickers hardness of the alloys A and B were measured to be 5.1 and 5.3 GPa, respectively. The ML predicted values were estimated at approximately 4.07 ± 0.28 and 6.04 ± 0.19 GPa, respectively, close to the experimental values.

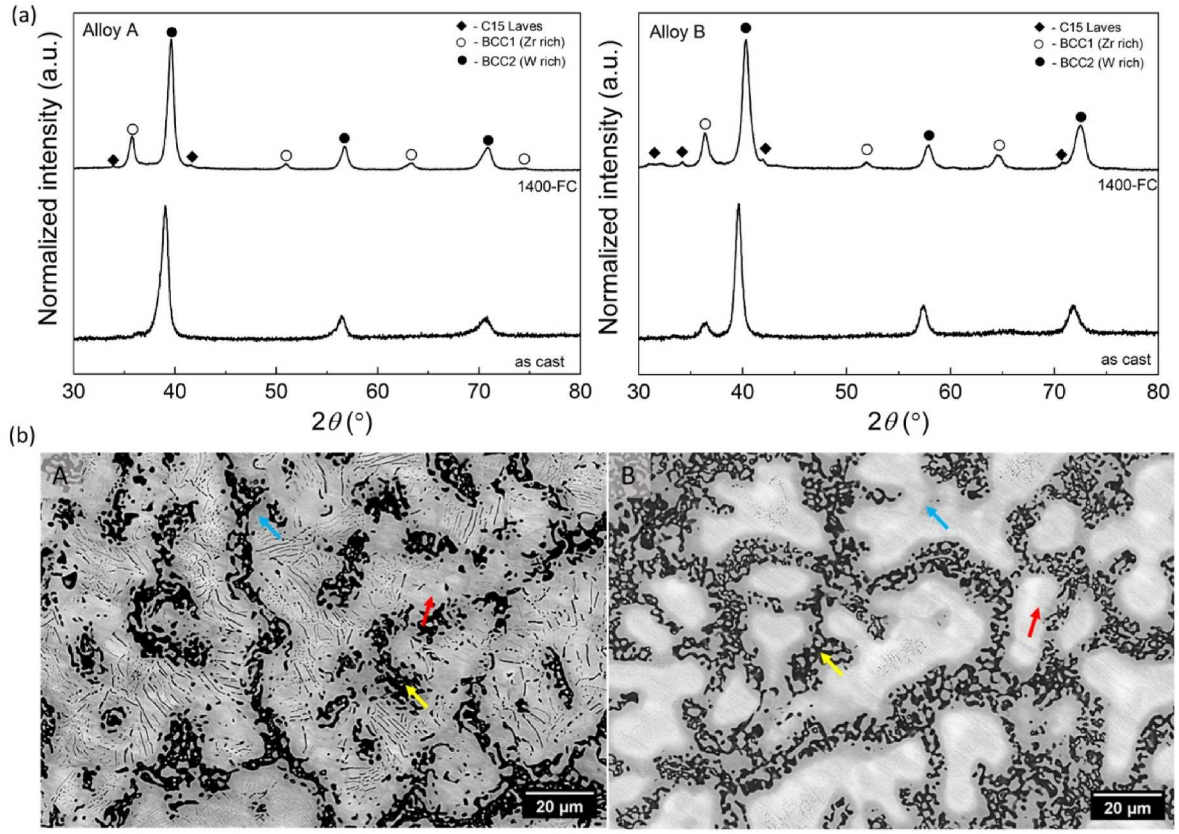

Fig. 1. (a) X-ray diffractogram of the alloys A and B in the as-cast and annealed condition showing the presence of two BCC solid solution and Laves phases and (b) SEM-BSE microstructure of alloys A and B after annealing. The blue, red, and yellow arrows indicate the grey, bright (D), and dark (ID) regions, respectively. 1400-FC in (a) denotes the sample annealed at 1400 °C for 48 h, followed by furnace cooling. (For interpretation of the references to color in this figure legend, the reader is referred to the Web version of this article.)

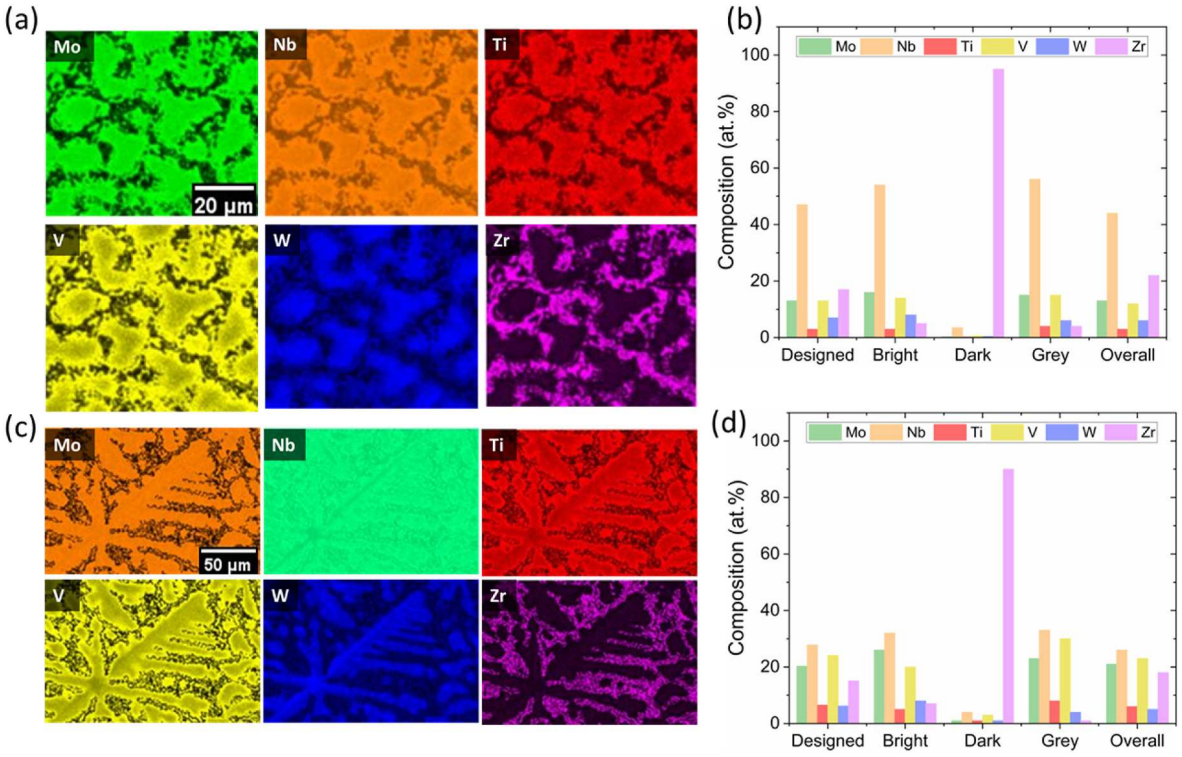

Fig. 2. Elemental mapping showing the distribution of various elements and EDS composition of different regions observed in Fig. 1(b) of alloys A(a-b) and B(c-d).

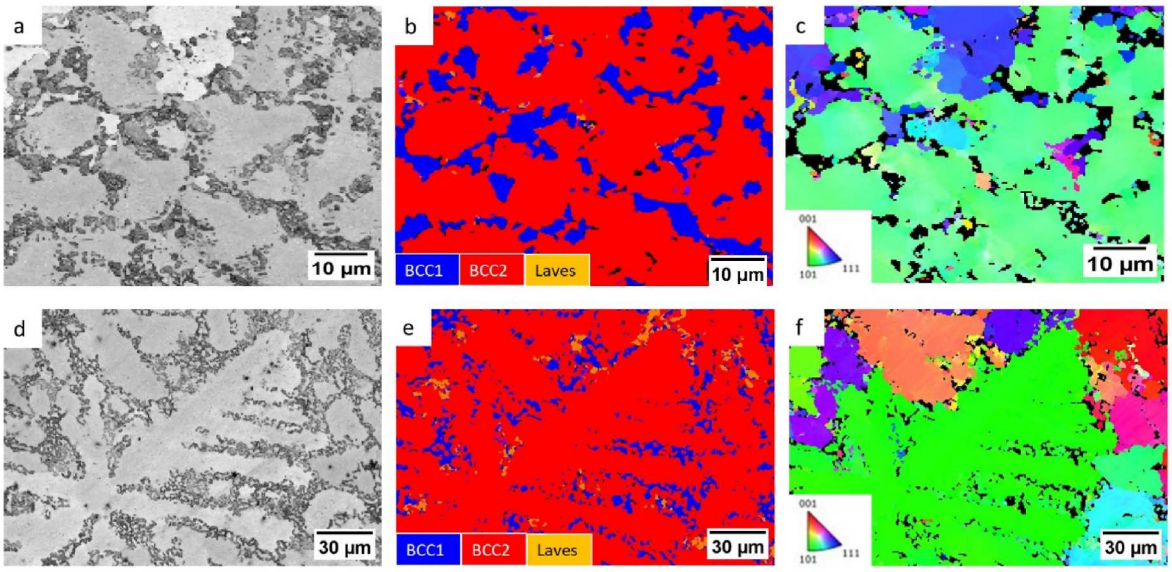

Fig. 3. SEM microstructure (a,d), the corresponding phase map (b,e), and IPF map (c,f) of alloys A and B, respectively.

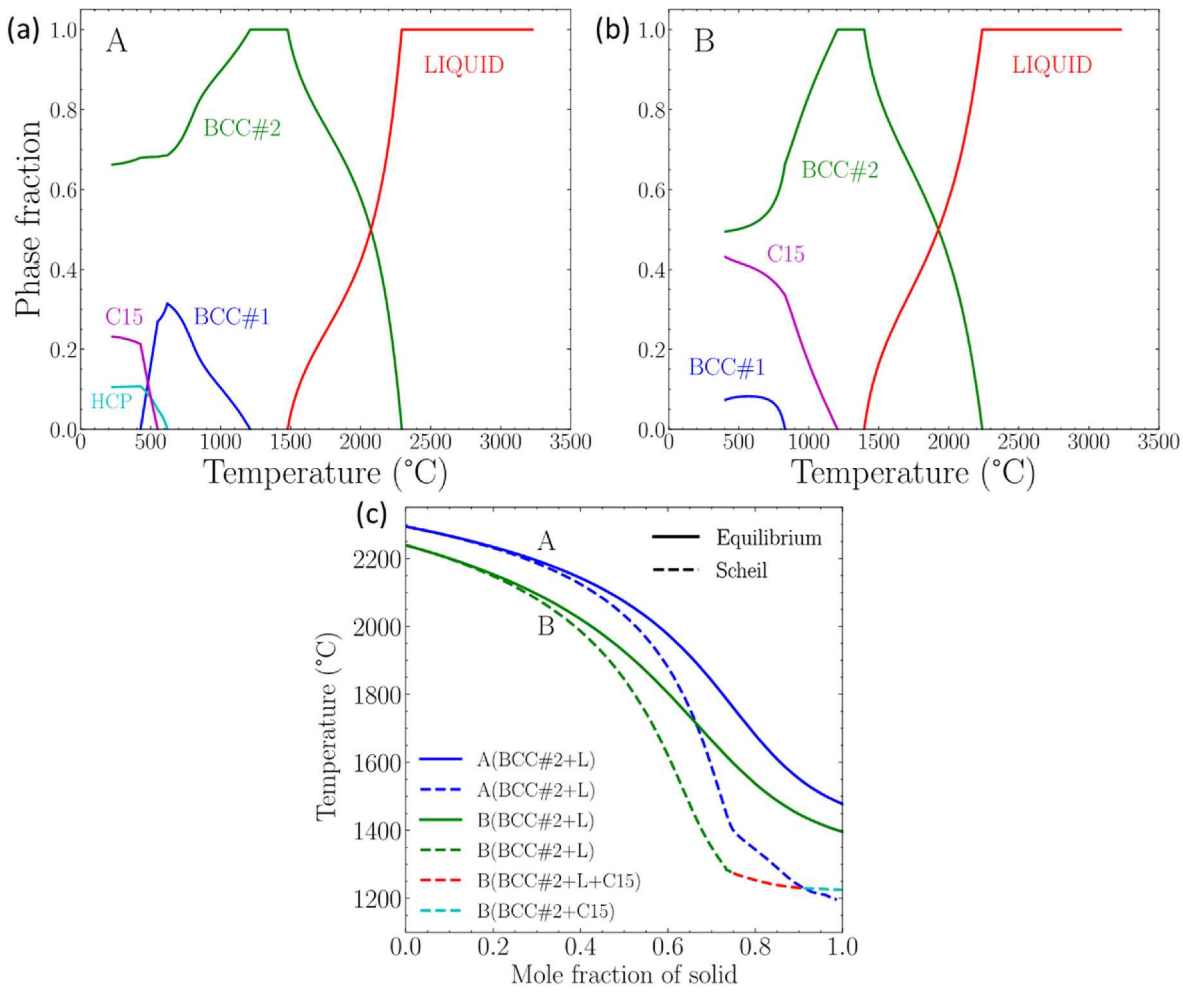

Fig. 4. (a–b) Phase fraction plot of alloys A and B (c) Solidification sequence of the alloys using Scheil simulation.

While the ensemble captured the expected order of higher hardness (Alloy B > A), the absolute values differed. The porosity in the annealed alloys resulted in lower compressive yield values. Incorporating porosity as a feature in the algorithm can improve the ML predictions.

Table 2
Phase formation criteria for alloys A and B.

Parameters	Alloy A	Alloy B	Inference	Ref
Entropy of mixing (ΔS_{mix}, R is gas constant)	1.48 R	1.66 R	Solid solution when $\Delta S_{mix} > 1.5R$	[48]
Enthalpy of mixing (ΔH_{mix}, kJ/mol)	−2.95	−3.55	Solid solution when $-15 \leq \Delta H_{mix} \leq 5$	[48]
Omega parameter $\Omega = \frac{T_m \Delta S_{mix}}{\lvert \Delta H_{mix} \rvert}$	10.69	9.77	Solid solution when $\Omega > 1.1$	[49]
Atomic size difference (δ, %)	5.46	5.76	Solid solution when $1 \leq \delta \leq 6$	[48]
Atomic packing parameter (γ)	1.19	1.19	Solid solution + IM/TCP formation when $\gamma > 1.175$	[50]
Electro-negativity $\Delta\chi_A$ (%)	5.6	6.31	TCP formation when $\Delta\chi_P >$ 0.133 and $\Delta\chi_A > 6$ %	[51]
$\Delta\chi_P$	0.24	0.25		
Valence electron concentration (VEC)	5	5.04	BCC when VEC <6.87	[52]

3.5.2. Room temperature three-point bend test and compression test

The Young's modulus of both alloys ranged from 120 to 150 GPa, and the mean flexural strength for alloys A and B were 440 and 340 MPa, respectively, as shown in Fig. 5(a). The critical elastic strain of the alloys A and B is 0.36 % ± 0.08 % and 0.26 % ± 0.05 %, respectively. The room temperature engineering stress-strain curves under compression are shown in Fig. 5(b). In both alloys, spallation was observed during compression. Alloy A exhibited better performance than alloy B, as indicated by the spallation location in Fig. 5(b). The microstructure shows the presence of pores, which are the main contributing factors to the low strength of these alloys (Supplementary sections S4 and S5). It is hypothesized that secondary processing techniques such as hot isostatic pressing would aid in closing the pores as well as breaking down the dendritic microstructure.

The CS ensemble model's RMSE (root mean square error) and R^2 scores are 0.34 GPa and 0.59, respectively. The predicted room temperature CS values for alloys A and B are 1630 ± 120 MPa and 1770 ± 110 MPa respectively, while the experimental values were observed to be between 1078-1404 MPa and 436–734 MPa, respectively. While the predictions using the simple descriptors mentioned in Section 2.1 might be a reasonable starting point, there is potential to reduce the disparity between the model and experiments by including more descriptive features. For instance, instead of binary features, CS may be better estimated by considering the volume fractions of the phases present in the sample. Additionally, performance can be improved by using advanced ML techniques like multi-task learning.

3.5.3. Hardness and modulus of the phases

Nanoindentation identified the contribution of each phase towards the overall mechanical strength through accelerated property maps (XPM), which provided the spatial distribution of hardness and modulus over the desired area of interest. Regions with all the phases were chosen for the NI study. The XPM of the alloys A and B are given in Fig. 6. The blue and red colors indicate the lower and upper limits of the values. The mean hardness and modulus of the various phases were calculated from their loading-unloading profiles from the NI data and are given in Table 3. For both alloys, the bright region (BCC2 phase) in the SEM image has relatively low hardness and high modulus, which indicates that the BCC2 phase, although stiffer, is more amenable to plastic deformation. The interface between the dark region (BCC1 phase) and the bright region (BCC2 phase, grey phase) has intermediate hardness and modulus, indicating a strong interface. The hardness and modulus values of both alloys are higher than the values reported for $(Ti44\text{-}V28\text{-}Nb14\text{-}Zr14)_{98.5}Mo_{1.5}$ [53]. This difference can primarily be attributed to the contribution of elements such as Mo and W.

3.5.4. Comparison of mechanical data of Mo-Nb-Ti-V-W-Zr with state-of-the-art RMCAs

The bending strength of the alloys A and B was 440 and 340 MPa, respectively, and the elastic modulus ranged from 120 to 150 GPa. Ti-Zr-Nb-Mo alloys exhibit higher bending strength and lower elastic modulus than those reported in this study [54]. The compressive yield strength of alloy A is similar to other RMCAs in Table 4. Although failure under compression may be challenging to identify, the failure stress was recognized at the instant spallation was observed; the mean compressive strength corresponding to spallation for alloys A and B were 1404 and 436 MPa, respectively, as indicated in Fig. 5(b). Alloy B exhibited lower strength and was more prone to spallation due to porosity. From Table 4, it can be inferred that alloy A has a preferable combination of hardness-strength and a lower density than MoNbTaW. Further, the ductility of these alloys can be improved via secondary processing conditions.

4. Conclusions

In this study, a multiphase RMCA with desired properties is designed using a data-driven alloy design approach. $Mo_{13}Nb_{47}Ti_3V_{13}W_7Zr_{17}$ (alloy A) and $Mo_{20.3}Nb_{0.278}Ti_{6.5}V_{24.1}W_{6.2}Zr_{15.1}$ (alloy B) show a hierarchical microstructure with 2 BCC solid solutions and a Laves phase, consistent with the CALPHAD and Scheil predictions. The BCC 2 phase

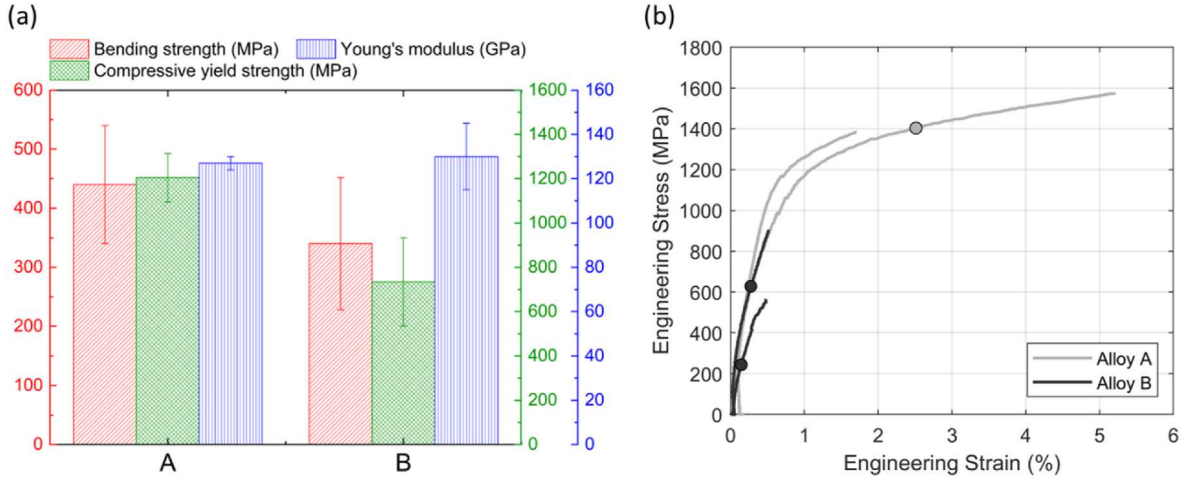

Fig. 5. (a) The elastic modulus, maximum stress under tension, and elastic strain obtained from room temperature three-point bend test. (b) Engineering stress-strain curve for compression. The dots represent when spalling on the surfaces first became visible.

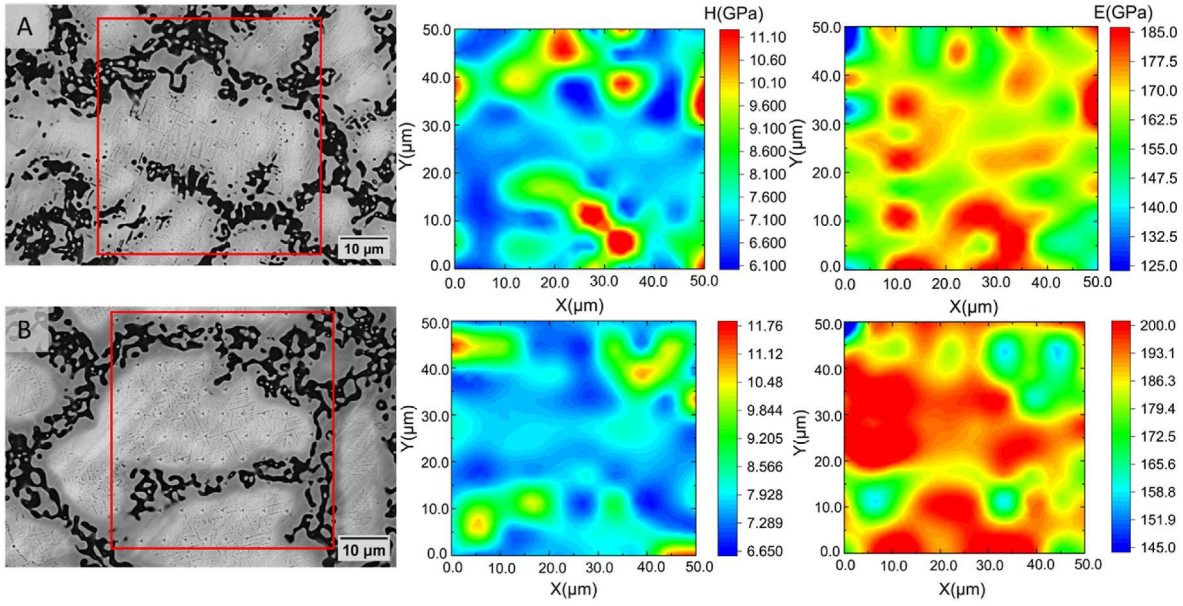

Fig. 6. Cross-sectional SEM micrograph of alloys A and B along with the corresponding hardness and modulus maps. The red box indicates the regions from which the hardness and modulus maps were taken. (For interpretation of the references to color in this figure legend, the reader is referred to the Web version of this article.)

Table 3
Hardness and modulus values of different phases obtained from NI-XPM.

Alloy	Property/Phases	BCC1	BCC2	Interface
A	**Hardness (GPa)**	9.6 ± 1.18	7.1 ± 0.4	8.4 ± 0.1
	Modulus (GPa)	170.2 ± 13.6	181.1 ± 7	165.5 ± 7.3
B	**Hardness (GPa)**	9.6 ± 1.5	7.8 ± 0.2	7.4 ± 0.7
	Modulus (GPa)	172 ± 7.7	197 ± 6	192.7 ± 5.3

(Zr depleted) has lower hardness and higher modulus than the BCC 1 phase, and the interface is relatively strong with intermediate properties between the BCC 1 and BCC 2 phases. Although the compressive yield strength of the alloys is not in complete agreement with the predicted values, an overall optimum density-strength combination of refractory alloys is achieved, indicating the excellent adaptability of the alloy design approach to other multicomponent systems. We envisage that integrating data-driven inverse design with experimental approaches will establish a new trajectory in advancing high-entropy refractory alloys. This holistic approach holds great promise for addressing the

Table 4
Summary of room temperature mechanical properties of a few RMCAs from the literature.

Alloys	Density (g/cm^3	Phases	Hardness (GPa)	Compressive yield strength (MPa)	% el.	Ref
$Zr_xNbMoTaW$	12.24[a]	2BCC	–	1354–1589	5–15	[55]
HfMoNbTaTiZr	9.96[a]	BCC	–	1512	12	[56]
HfNbTaTiZr	9.91[a]	BCC	–	929	>50	
HfMoTaTiZr	10.24[a]	BCC	–	1600	4	
HfMoNbTiZr	8.62[a]	BCC	–	1351	20	
HfMoNbTaZr	11.05[a]	BCC	–	1524	16	
HfMoNbTaTi	10.65[a]	BCC	–	1369	27	
Nb-Mo-Zr-Al	7.56–8.58	BCC + HCP + Al_3Zr_5	–	587–1240		[46]
MoNbVW	11.1	BCC	6 ± 0.2	1243 ± 49		[57]
MoNbVTi	7.4	BCC	4 ± 0.1	1210 ± 36		
$Mo_{30}Nb_{30}V_{30}Ti_{10}$	7.9	BCC	4 ± 0.2	1441 ± 39		
MoNbVWTi	9.8	BCC	5 ± 0.1	1289 ± 42		
NbTiVZr	6.52	BCC	3.29			[20]
$NbTiV_2Zr$	6.34	3BCC	2.99			[21]
$Ti_2VNbMoZr_x$	6.7	2BCC	4.1	1287–1421	27–30	[58]
$TiMoNbZr_x$	7.46[a]	BCC	3.9–5	1109–1314	8–12	[59]
$TiZrNbMoV_x$	7.2[a]	2BCC	–	1500	10–12	[60]
HfNbTaTiZr	9.9[a]	BCC	–	929		[61]
HfNbTaTiZrW	11.46[a]	2BCC	–	1550	26.3	[62]
HfNbTaTiZrMoW	11.28[a]	2BCC	–	1637	15.5	
NbTiVZr	6.43	BCC	–	967	>50	[63]
MoNbTaTiW	11.84[a]	BCC	–	1343	14	[64]
MoNbTaTiVW	10.88[a]	BCC	–	1515	11	
MoNbTaW	12.36	BCC	4.26	1058	2.6	[65]
MoNbTaVW	13.75	BCC	5.23	1246	1.7	
$W_x(TaVZr)_{100-x}$	10–11.8	BCC + HCP + Laves	5.6–6.4	1680–1985	1.2–3.2	[66]
$Mo_{13}Nb_{47}Ti_3V_{13}W_7Zr_{17}$	7.76	2BCC + Laves	5.1	1078–1404	2–5	Present work
$Mo_{20.3}Nb_{27.8}Ti_{6.5}V_{24.1}W_{6.2}Zr_{15.1}$	8.32	2BCC + Laves	5.3	436–734	1–2	Present work

[a] Density of the alloys is calculated using the rule of mixtures.

pressing challenges in high-temperature materials science and engineering, ultimately driving advancements in various industrial and technological sectors.

CRediT authorship contribution statement

Lavanya Raman: Writing – review & editing, Writing – original draft, Validation, Methodology, Investigation, Formal analysis, Data curation, Conceptualization. **Arindam Debnath:** Writing – review & editing, Writing – original draft, Validation, Investigation, Formal analysis, Data curation. **Erik Furton:** Writing – review & editing, Writing – original draft, Validation, Investigation, Formal analysis, Data curation. **Shuang Lin:** Writing – original draft, Methodology, Investigation, Formal analysis, Data curation. **Adam Krajewski:** Writing – original draft, Validation, Software, Methodology, Investigation, Data curation. **Subrata Ghosh:** Methodology. **Na Liu:** Data curation, Methodology. **Marcia Ahn:** Writing – original draft, Validation, Investigation, Formal analysis, Data curation. **Bed Poudel:** Project administration. **Shunli Shang:** Visualization, Validation, Supervision, Investigation, Formal analysis, Data curation, Conceptualization. **Shashank Priya:** Writing – review & editing, Visualization, Supervision, Resources, Project administration, Funding acquisition, Conceptualization. **Zi-Kui Liu:** Writing – review & editing, Visualization, Validation, Supervision, Software, Resources, Project administration, Funding acquisition, Conceptualization. **Allison M. Beese:** Writing – review & editing, Writing – original draft, Visualization, Validation, Supervision, Resources, Project administration, Methodology, Investigation, Formal analysis, Conceptualization. **Wesley Reinhart:** Visualization, Validation, Supervision, Software, Resources, Project administration, Investigation, Formal analysis, Conceptualization. **Wenjie Li:** Writing – review & editing, Validation, Supervision, Project administration, Investigation, Conceptualization.

Declaration of competing interest

The authors declare that they have no known competing financial interests or personal relationships that could have appeared to influence the work reported in this paper.

Acknowledgments

The authors thank Dr. Kim Hojong and Dr. Jarrod Gesualdi for helping with the arc melting facility. The authors acknowledge the Department of Energy/Advanced Research Projects Agency-Energy (ARPA-E) support under award No. DE-AR0001435.

Appendix A. Supplementary data

Supplementary data to this article can be found online at https://doi.org/10.1016/j.msea.2024.147475.

Data availability

Data will be made available on request.

References

[1] E.M. Savitskii, G.S. Burkhanov, Physical metallurgy of refractory metals and alloys, New York - London, https://doi.org/10.1007/978-1-4684-1572-8, 1995.
[2] P. Sathiyamoorthi, H.S. Kim, High-entropy alloys with heterogeneous microstructure: processing and mechanical properties, Prog. Mater. Sci. 123 (2022) 100709, https://doi.org/10.1016/j.pmatsci.2020.100709.
[3] E. Ma, X. Wu, Tailoring heterogeneities in high-entropy alloys to promote strength–ductility synergy, Nat. Commun. 10 (2019) 1–10, https://doi.org/10.1038/s41467-019-13311-1.
[4] X. Wu, Y. Zhu, Heterogeneous materials: a new class of materials with unprecedented mechanical properties, Mater. Res. Lett. 5 (2017) 527–532, https://doi.org/10.1080/21663831.2017.1343208.
[5] Z. Li, D. Raabe, Strong and ductile non-equiatomic high-entropy alloys: design, processing, microstructure, and mechanical properties, Jom 69 (2017) 2099–2106, https://doi.org/10.1007/s11837-017-2540-2.
[6] K.G. Pradeep, C.C. Tasan, M.J. Yao, Y. Deng, H. Springer, D. Raabe, Non-equiatomic high entropy alloys: approach towards rapid alloy screening and property-oriented design, Mater. Sci. Eng., A 648 (2015) 183–192, https://doi.org/10.1016/j.msea.2015.09.010.
[7] Z. Pei, S. Zhao, M. Detrois, P.D. Jablonski, J.A. Hawk, D.E. Alman, M. Asta, A. M. Minor, M.C. Gao, Theory-guided design of high-entropy alloys with enhanced strength-ductility synergy, Nat. Commun. 14 (2023), https://doi.org/10.1038/s41467-023-38111-6.
[8] O.N. Senkov, J.D. Miller, D.B. Miracle, C. Woodward, Accelerated exploration of multi-principal element alloys with solid solution phases, Nat. Commun. 6 (2015) 1–10, https://doi.org/10.1038/ncomms7529.
[9] G. Ouyang, P. Singh, R. Su, D.D. Johnson, M.J. Kramer, J.H. Perepezko, O. N. Senkov, D. Miracle, J. Cui, Design of refractory multi-principal-element alloys for high-temperature applications, npj Comput. Mater. 9 (2023) 1–10, https://doi.org/10.1038/s41524-023-01095-4.
[10] S. Risal, W. Zhu, P. Guillen, L. Sun, Improving phase prediction accuracy for high entropy alloys with Machine learning, Comput. Mater. Sci. 192 (2021) 110389, https://doi.org/10.1016/j.commatsci.2021.110389.
[11] K. Kaufmann, K.S. Vecchio, Searching for high entropy alloys: a machine learning approach, Acta Mater. 198 (2020) 178–222, https://doi.org/10.1016/j.actamat.2020.07.065.
[12] A. Debnath, A.M. Krajewski, H. Sun, S. Lin, M. Ahn, W. Li, S. Priya, J. Singh, S. Shang, A.M. Beese, Z.-K. Liu, W.F. Reinhart, Generative deep learning as a tool for inverse design of high entropy refractory alloys, J. Mater. Inform. (2021) 1–13, https://doi.org/10.20517/jmi.2021.05.
[13] A.M. Krajewski, A. Debnath, S. Lin, M. Ahn, H. Sun, W. Reinhart, A. Beese, Z.-K. Liu, in: ULtrahigh TEmperature Refractory Alloys (ULTERA) Database of High Entropy Alloys, 2023, https://doi.org/10.5281/zenodo.7566415.
[14] L. Qiao, Z. Lai, Y. Liu, A. Bao, J. Zhu, Modelling and prediction of hardness in multi-component alloys: a combined machine learning, first principles and experimental study, J. Alloys Compd. 853 (2021) 156959, https://doi.org/10.1016/j.jallcom.2020.156959.
[15] S.A. Giles, H. Shortt, P.K. Liaw, D. Sengupta, Yield strength-plasticity trade-off and uncertainty quantification for machine-learning-based design of refractory high-Entropy Alloys. https://doi.org/10.21203/rs.3.rs-2943316/v1.
[16] S. Hou, M. Sun, M. Bai, D. Lin, Y. Li, W. Liu, A hybrid prediction frame for HEAs based on empirical knowledge and machine learning, Acta Mater. 228 (2022), https://doi.org/10.1016/j.actamat.2022.117742.
[17] C. Wen, Y. Zhang, C. Wang, D. Xue, Y. Bai, S. Antonov, L. Dai, T. Lookman, Y. Su, Machine learning assisted design of high entropy alloys with desired property, Acta Mater. 170 (2019) 109–117, https://doi.org/10.1016/j.actamat.2019.03.010.
[18] R.R. Eleti, T. Bhattacharjee, A. Shibata, N. Tsuji, Unique deformation behavior and microstructure evolution in high temperature processing of HfNbTaTiZr refractory high entropy alloy, Acta Mater. 171 (2019) 132–145, https://doi.org/10.1016/j.actamat.2019.04.018.
[19] O.N. Senkov, D.B. Miracle, K.J. Chaput, J.P. Couzinie, Development and exploration of refractory high entropy alloys - a review, J. Mater. Res. 33 (2018) 3092–3128, https://doi.org/10.1557/jmr.2018.153.
[20] O.N. Senkov, S.V. Senkova, C. Woodward, D.B. Miracle, Low-density, refractory multi-principal element alloys of the Cr-Nb-Ti-V-Zr system: microstructure and phase analysis, Acta Mater. 61 (2013) 1545–1557, https://doi.org/10.1016/j.actamat.2012.11.032.
[21] O.N. Senkov, S. V Senkova, D.B. Miracle, C. Woodward, Materials Science & Engineering A Mechanical properties of low-density , refractory multi-principal element alloys of the Cr – Nb – Ti – V – Zr system, Mater. Sci. Eng., A 565 (2013) 51–62, https://doi.org/10.1016/j.msea.2012.12.018.
[22] O.N. Senkov, G.B. Wilks, D.B. Miracle, C.P. Chuang, P.K. Liaw, Refractory high-entropy alloys, Intermetallics 18 (2010) 1758–1765, https://doi.org/10.1016/j.intermet.2010.05.014.
[23] B. Yin, F. Maresca, W.A. Curtin, Vanadium is an optimal element for strengthening in both fcc and bcc high-entropy alloys, Acta Mater. 188 (2020) 486–491, https://doi.org/10.1016/j.actamat.2020.01.062.
[24] A.M. Krajewski, A. Debnath, S. Lin, M. Ahn, H. Sun, W. Reinhart, A. Beese, Z.-K. Liu, in: ULtrahigh TEmperature Refractory Alloys (ULTERA) Database of High Entropy Alloys, 2023, https://doi.org/10.5281/zenodo.7566415.
[25] W. Li, L. Raman, A. Debnath, M. Ahn, S. Lin, A.M. Krajewski, S. Shang, S. Priya, W. F. Reinhart, Z.-K. Liu, A.M. Beese, Design and validation of refractory alloys using machine learning, CALPHAD, and experiments, Int. J. Refract. Metals Hard Mater. 121 (2024) 106673, https://doi.org/10.1016/j.ijrmhm.2024.106673.
[26] S. Feng, H. Fu, H. Zhou, Y. Wu, Z. Lu, H. Dong, A general and transferable deep learning framework for predicting phase formation in materials, npj Comput. Mater. 7 (2021), https://doi.org/10.1038/s41524-020-00488-z.
[27] A. Debnath, W.F. Reinhart, Investigating representation schemes for surrogate modeling of High Entropy Alloys, Comput. Mater. Sci. 230 (2023), https://doi.org/10.1016/j.commatsci.2023.112460.
[28] J.B. Nelson, D.P. Riley, An experimental investigation of extrapolation methods in the derivation of accurate unit-cell dimensions of crystals, Proc. Phys. Soc. 57 (1945) 160–177, https://doi.org/10.1088/0959-5309/57/3/302.
[29] B. Sundman, B. Jansson, J.O. Andersson, The Thermo-Calc databank system, Calphad 9 (1985) 153–190.
[30] N. Saunders, A.P. Miodownik, CALPHAD (Calculation of Phase Diagrams): A Comprehensive Guide, Elsevier, 1998.

[31] J. Bratberg, K. Frisk, A thermodynamic analysis of the Mo-V and Mo-V-C system, Calphad 26 (2002) 459–476, https://doi.org/10.1016/S0364-5916(02)00057-3.
[32] K. Frisk, P. Gustafson, An assessment of the Cr-Mo-W system, Calphad 12 (1988) 247–254, https://doi.org/10.1016/0364-5916(88)90004-1.
[33] R. Jerlerud Pérez, B. Sundman, Thermodynamic assessment of the Mo–Zr binary phase diagram, Calphad 27 (2003) 253–262, https://doi.org/10.1016/j.calphad.2003.09.003.
[34] Y. Zhang, H. Liu, Z. Jin, Thermodynamic assessment of the Nb-Ti system, Calphad 25 (2001) 305–317, https://doi.org/10.1016/S0364-5916(01)00051-7.
[35] K.C.H. Kumar, P. Wollants, L. Delaey, Thermodynamic calculation of Nb-Ti-V phase diagram, Calphad 18 (1994) 71–79, https://doi.org/10.1016/0364-5916(94)90008-6.
[36] A. Fernändez Guillermet, Thermodynamic Analysis of the Stable Phases in the Zr - Nb System and Calculation of the Phase Diagram/Thermodynamische Analyse der stabilen Phasen im System Zr - Nb und Berechnung des Zustandsdiagramms, Int. J. Mater. Res. 82 (1991) 478–487, https://doi.org/10.1515/ijmr-1991-820609.
[37] G. Ghosh, Thermodynamic and kinetic modeling of the Cr-Ti-V system, J. Phase Equil. 23 (2002) 310–328, https://doi.org/10.1361/105497102770331569.
[38] S. Jonsson, Reevaluation of the Ti-W system and prediction of the Ti-W-N phase diagram, Int. J. Mater. Res. 87 (1996) 784–787, https://doi.org/10.1515/ijmr-1996-871008.
[39] K.C. Hari Kumar, P. Wollants, L. Delacy, Thermodynamic assessment of the Ti–Zr system and calculation of the Nb–Ti–Zr phase diagram, J. Alloys Compd. 206 (1994) 121–127, https://doi.org/10.1016/0925-8388(94)90019-1.
[40] X.-S. Zhao, G.-H. Yuan, M.-Y. Yao, Q. Yue, J.-Y. Shen, First-principles calculations and thermodynamic modeling of the V–Zr system, Calphad 36 (2012) 163–168, https://doi.org/10.1016/j.calphad.2011.07.003.
[41] C. Guo, C. Li, S. Shang, Z. Du, Thermodynamic description of the Ta–W–Zr system, Int. J. Mater. Res. 105 (2014) 1048–1056, https://doi.org/10.3139/146.111125.
[42] W. Xiong, Y. Du, Y. Liu, B.Y. Huang, H.H. Xu, H.L. Chen, Z. Pan, Thermodynamic assessment of the Mo–Nb–Ta system, Calphad 28 (2004) 133–140, https://doi.org/10.1016/j.calphad.2004.07.002.
[43] K. Santhy, K.C. Hari Kumar, Thermodynamic assessment of Mo-Ni-Ti ternary system by coupling first-principle calculations with CALPHAD approach, Intermetallics 18 (2010) 1713–1721, https://doi.org/10.1016/j.intermet.2010.05.008.
[44] E. Scheil, Bemerkungen zur Schichtkristallbildung, Int. J. Mater. Res. 34 (1942) 244–253, https://doi.org/10.1515/IJMR-1942-340303.
[45] A. Debnath, L. Raman, W. Li, A.M. Krajewski, M. Ahn, S. Lin, S. Shang, A.M. Beese, Z.-K. Liu, W.F. Reinhart, Comparing forward and inverse design paradigms: a case study on refractory high-entropy alloys, J. Mater. Res. 38 (2023) 4107–4117, https://doi.org/10.1557/s43578-023-01122-6.
[46] O.N. Senkov, S.I. Rao, T.M. Butler, T.I. Daboiku, K.J. Chaput, Microstructure and properties of Nb-Mo-Zr based refractory alloys, Int. J. Refract. Metals Hard Mater. 92 (2020) 105321, https://doi.org/10.1016/j.ijrmhm.2020.105321.
[47] O.N. Senkov, S. Rao, K.J. Chaput, C. Woodward, Compositional effect on microstructure and properties of NbTiZr-based complex concentrated alloys, Acta Mater. 151 (2018) 201–215, https://doi.org/10.1016/j.actamat.2018.03.065.
[48] Y. Zhang, Y.J. Zhou, J.P. Lin, G.L. Chen, P.K. Liaw, Solid-solution phase formation rules for multi-component alloys, Adv. Eng. Mater. 10 (2008) 534–538, https://doi.org/10.1002/adem.200700240.
[49] Y. Zhang, X. Yang, P.K. Liaw, Alloy design and properties optimization of high-entropy alloys, Jom 64 (2012) 830–838, https://doi.org/10.1007/s11837-012-0366-5.
[50] N. Yurchenko, N. Stepanov, G. Salishchev, Laves-phase formation criterion for high-entropy alloys, Mater. Sci. Technol. 33 (2017) 17–22, https://doi.org/10.1080/02670836.2016.1153277.
[51] M.G. Poletti, L. Battezzati, Electronic and thermodynamic criteria for the occurrence of high entropy alloys in metallic systems, Acta Mater. 75 (2014) 297–306, https://doi.org/10.1016/j.actamat.2014.04.033.
[52] S. Guo, C. Ng, J. Lu, C.T. Liu, Effect of valence electron concentration on stability of fcc or bcc phase in high entropy alloys, J. Appl. Phys. 109 (2011), https://doi.org/10.1063/1.3587228.
[53] Y. Jia, C. Ren, S. Wu, Y. Mu, L. Xu, Y. Jia, W. Yan, J. Yi, G. Wang, Multistage strain-hardening behavior of ultrastrong and ductile lightweight refractory complex-concentrated alloys, J. Mater. Sci. Technol. 149 (2023) 73–87, https://doi.org/10.1016/j.jmst.2022.12.011.
[54] K.-K. Wong, H.-C. Hsu, S.-C. Wu, W.-F. Ho, Structure and properties of Ti-rich Ti–Zr–Nb–Mo medium-entropy alloys, J. Alloys Compd. 868 (2021) 159137, https://doi.org/10.1016/j.jallcom.2021.159137.
[55] T. Li, W. Jiao, J. Miao, Y. Lu, E. Guo, T. Wang, T. Li, P.K. Liaw, A novel ZrNbMoTaW refractory high-entropy alloy with in-situ forming heterogeneous structure, Mater. Sci. Eng., A 827 (2021) 142061, https://doi.org/10.1016/j.msea.2021.142061.
[56] K.K. Tseng, C.C. Juan, S. Tso, H.C. Chen, C.W. Tsai, J.W. Yeh, Effects of Mo, Nb, Ta, Ti, and Zr on mechanical properties of equiatomic Hf-Mo-Nb-Ta-Ti-Zr alloys, Entropy 21 (2019) 1–14, https://doi.org/10.3390/e21010015.
[57] M. Regenberg, G. Hasemann, M. Wilke, T. Halle, M. Krüger, Microstructure evolution and mechanical properties of refractory Mo-Nb-V-W-Ti high-entropy alloys, Metals 10 (2020) 1–13, https://doi.org/10.3390/met10111530.
[58] T. Li, J. Miao, Y. Lu, T. Wang, T. Li, Effect of Zr on the as-cast microstructure and mechanical properties of lightweight Ti2VNbMoZrx refractory high-entropy alloys, Int. J. Refract. Metals Hard Mater. 103 (2022) 105762, https://doi.org/10.1016/j.ijrmhm.2021.105762.
[59] G. Chen, Y. Xiao, X. Ji, X. Liang, Y. Hu, Z. Cai, J. Liu, Y. Tong, Effects of Zr content on the microstructure and performance of TiMoNbZrx high-entropy alloys, Metals 11 (2021), https://doi.org/10.3390/met11081315.
[60] X. Yang, Y. Zhang, Prediction of high-entropy stabilized solid-solution in multi-component alloys, Mater. Chem. Phys. 132 (2012) 233–238, https://doi.org/10.1016/j.matchemphys.2011.11.021.
[61] L.Y. Tian, G. Wang, J.S. Harris, D.L. Irving, J. Zhao, L. Vitos, Alloying effect on the elastic properties of refractory high-entropy alloys, Mater. Des. 114 (2017) 243–252, https://doi.org/10.1016/j.matdes.2016.11.079.
[62] M. Wang, Z. Ma, Z. Xu, X. Cheng, Microstructures and mechanical properties of HfNbTaTiZrW and HfNbTaTiZrMoW refractory high-entropy alloys, J. Alloys Compd. 803 (2019) 778–785, https://doi.org/10.1016/j.jallcom.2019.06.138.
[63] Y. Jia, L. Zhang, P. Li, X. Ma, L. Xu, S. Wu, Y. Jia, G. Wang, Microstructure and mechanical properties of Nb–Ti–V–Zr refractory medium-entropy alloys, Front Mater 7 (2020) 1–11, https://doi.org/10.3389/fmats.2020.00172.
[64] Z.D. Han, N. Chen, S.F. Zhao, L.W. Fan, G.N. Yang, Y. Shao, K.F. Yao, Effect of Ti additions on mechanical properties of NbMoTaW and VNbMoTaW refractory high entropy alloys, Intermetallics 84 (2017) 153–157, https://doi.org/10.1016/j.intermet.2017.01.007.
[65] O.N. Senkov, G.B. Wilks, J.M. Scott, D.B. Miracle, Mechanical properties of Nb25Mo25Ta 25W25 and V20Nb20Mo 20Ta20W20 refractory high entropy alloys, Intermetallics 19 (2011) 698–706, https://doi.org/10.1016/j.intermet.2011.01.004.
[66] J. Zhang, S. Chen, J. Liu, Z. Qing, Y. Wu, Microstructure and mechanical properties of novel high-strength, low-activation wx(TaVZr)100−x (x = 5, 10, 15, 20, 25) refractory high entropy alloys, Entropy 24 (2022), https://doi.org/10.3390/e24101342.